

CrossMark
click for updatesCite this: *RSC Adv.*, 2016, 6, 111882

Stable nickel-substituted spinel cathode material ($\text{LiMn}_{1.9}\text{Ni}_{0.1}\text{O}_4$) for lithium-ion batteries obtained by using a low temperature aqueous reduction technique

Niki Kunjuzwa,^{ab} Mesfin A. Kebede,^{*a} Kenneth I. Ozoemena^{ab} and Mkhulu K. Mathe^{*a}

A nickel substituted spinel cathode material ($\text{LiMn}_{1.9}\text{Ni}_{0.1}\text{O}_4$) with enhanced electrochemical performance was successfully synthesized by using a locally-sourced, low-cost manganese precursor, electrolytic manganese dioxide (EMD), and $\text{NiSO}_4 \cdot 6\text{H}_2\text{O}$ as a nickel source by means of a low temperature aqueous reduction synthesis technique. This synthesis protocol is convenient to scale up the production of the spinel cathode material, with minimal nickel content ($\text{Ni} = 0.1$) in the structure, for lithium-ion battery applications. Ni-ions substituting Mn-ions was confirmed using XRD, EDS, XPS and electrochemical performance studies. $\text{LiMn}_{1.9}\text{Ni}_{0.1}\text{O}_4$ materials showed an octahedral shape with clearly exposed (111) facets that enhanced the Li-ion kinetics and improved the cycling performance compared to the pristine spinel sample (LiMn_2O_4). The $\text{LiMn}_{1.9}\text{Ni}_{0.1}\text{O}_4$ sample exhibited superior capacity retention by retaining 84% of its initial capacity (128 mA h g^{-1}) whereas pristine LiMn_2O_4 retained only 52% of its initial capacity (137 mA h g^{-1}). XPS confirmed that the $\text{Mn}^{3+}/\text{Mn}^{4+}$ ratio changed with nickel substitution and favored the suppression of capacity fading. The study clearly suggests that the integration of small amounts of Ni into the spinel structure is able to eliminate the disadvantageous Jahn–Teller effects in the LiMn_2O_4 .

Received 15th September 2016
Accepted 20th November 2016

DOI: 10.1039/c6ra23052k

www.rsc.org/advances

Introduction

Lithium-ion battery (LIB) technology is well-developed for portable electronic devices (like cellphones, laptops, iPads, etc.) which have been widely used. However, to implement LIBs for large-scale high-power systems such as plug-in hybrid electric vehicles (PHEVs) or plug-in electric vehicles (PEVs), there is a great need to increase the energy and power capabilities of these batteries.^{1–5} Nickel-substituted LiMn_2O_4 (i.e., $\text{LiMn}_{2-x}\text{Ni}_x\text{O}_4$) has emerged as one of the promising spinel cathode materials for lithium-ion batteries. A member of the family is the high-voltage spinel $\text{LiMn}_{1.5}\text{Ni}_{0.5}\text{O}_4$ (LMNO) is considered as one of the most promising cathode materials for Li-ion batteries.^{6,7} In comparison with the commercial LiCoO_2 positive electrode, $\text{LiMn}_{1.5}\text{Ni}_{0.5}\text{O}_4$ has been shown to intercalate–deintercalate Li^+ ions at very high potential ($E = 4.7 \text{ V vs. Li}^+/\text{Li}$).⁸ It has a large high intrinsic rate capability offered by the 3-dimensional lithium-ion diffusion in the spinel lattice. Besides, it is much safer, low-cost, and greener.⁹ There is a continued need to reduce the cost of the $\text{LiMn}_{1.5}\text{Ni}_{0.5}\text{O}_4$ by the use of low-cost synthesis method, the use of low-cost manganese precursor

(such as the electrolytic manganese oxide, EMD) as well as drastic reduction in the amount of the expensive nickel in the structure ($\text{Ni} < 0.5$), without compromising its advantageous properties.

In this work, the preparation and electrochemical properties of $\text{LiMn}_{1.9}\text{Ni}_{0.1}\text{O}_4$ cathode materials containing very small amount of nickel ($x = 0.1$) and using EMD precursor have been investigated. The spinel cathode material was chosen due to its low toxicity, abundant material source and its high specific capacity of 148 mA h g^{-1} . The commercial spinel cathode material (LiMn_2O_4) is a well-studied cathode system for LIB with the potential to serve as an alternative to the toxic and expensive LiCoO_2 . However, the main challenge with LiMn_2O_4 is the capacity fading due to Jahn–Teller distortion^{10–12} in the 3 V region,¹³ which is due to the generation of new phases during cycling and disproportionation reaction. In order to overcome this limitation, we have adapted a Ni-doping strategy. Literature reports have shown that doping with a small amount of Cr^{3+} , Ni^{2+} and Al^{3+} can stabilize the spinel structure of LiMn_2O_4 and provides high operating voltage above 4.7 V, suppress the Jahn–Teller effect, and improve the cycling properties.^{14–16} Although the use of small amount of nickel in the structure (i.e., $\text{Ni} < 0.5$) has rarely been studied, it has been established that $\text{Ni} = 0.1$ provides the best electrochemistry.¹² Therefore, there is a need to further explore the performance of this spinel using new low-cost synthetic routes.

^aEnergy Materials, Materials Science and Manufacturing, Council for Scientific and Industrial Research (CSIR), Pretoria, 0001, South Africa. E-mail: kmathe@csir.co.za; mkebede@csir.co.za; Fax: +27 128412135; Tel: +27 128413665; +27 128413588

^bMolecular Sciences Institute, School of Chemistry, University of the Witwatersrand, Private Bag 3, P O WITS 2050, Johannesburg, South Africa

Various synthetic routes have been followed to synthesize different spinel cathode materials, including solid state,¹⁷ combustion,¹⁵ co-precipitation,¹⁸ sol-gel method¹⁹ and modified pechini.²⁰ Unfortunately these methods require elevated temperatures as high as 700–900 °C. Further, $\text{LiMn}_{2-x}\text{Ni}_x\text{O}_4$ synthesized by the solid-state method is often accompanied by the formation of $\text{Li}_x\text{Ni}_x\text{O}$ impurity phases which causes capacity fading. The crystallinity of the materials is also poor and leads to the dissolution of crystal faces by an electrolyte which deteriorates the rate capability. The techniques based on the processes of co-precipitation can give single phase $\text{LiMn}_{2-x}\text{Ni}_x\text{O}_4$ at lower temperatures. However, these methods involve the use of expensive reagents with complex process.²¹

In this work, for the first time, we opted for a low temperature aqueous reduction method²² to synthesize $\text{LiMn}_{1.9}\text{Ni}_{0.1}\text{O}_4$ cathode materials. We have used $\text{NiSO}_4 \cdot 6(\text{H}_2\text{O})$ as the nickel source and locally-produced low-cost EMD as the Mn source. This synthesis method not only has the advantage of using a locally-produced low-cost EMD but can also be a viable replacement to co-precipitation technique.

Experimental

Materials and preparation

Electrolytic manganese dioxide (EMD) from a South African supplier (Delta EMD Pty Ltd) and $\text{LiOH} \cdot \text{H}_2\text{O}$, $\text{NiSO}_4 \cdot 6(\text{H}_2\text{O})$, glucose from Sigma Aldrich were used for the synthesis of spinel $\text{LiMn}_{2-x}\text{Ni}_x\text{O}_4$ ($x = 0$ and 0.1) cathode materials.

Both $\text{LiMn}_{1.9}\text{Ni}_{0.1}\text{O}_4$ and its pristine material, LiMn_2O_4 (for comparison) were prepared using a facile and low temperature aqueous reduction synthesis method by employing electrolytic manganese dioxide (EMD), $\text{LiOH} \cdot \text{H}_2\text{O}$, $\text{NiSO}_4 \cdot 6(\text{H}_2\text{O})$ (for the Ni-doped sample) and glucose as a reducing agent. Briefly, a stoichiometric amount of $\text{LiOH} \cdot \text{H}_2\text{O}$, EMD and $\text{NiSO}_4 \cdot 6(\text{H}_2\text{O})$ (for the $\text{LiMn}_{1.9}\text{Ni}_{0.1}\text{O}_4$ sample) was dissolved in 60 mL of double-distilled water by continuous stirring at a temperature of 80 °C. After 1 h, the appropriate amount of glucose dissolved in 20 mL of double-distilled water was added to the mixture. The stirring was continued for a further 8 h at 80 °C until the reaction was complete. The slurry was allowed to cool and settle for 12 h. After decanting, the product was washed several times with distilled water and dried at 120 °C. The resultant powder was calcined at 780 °C for 20 h in air and then cooled to room temperature naturally in the furnace. The purpose of further calcination at 780 °C to 20 h is to generate the required phase structure and composition in the $\text{LiMn}_{2-x}\text{Ni}_x\text{O}_4$ product ($x = 0$ and 0.1). In both samples, the same method of synthesis was adopted.

Equipment and procedure

The morphology of the samples $\text{LiMn}_{2-x}\text{Ni}_x\text{O}_4$ ($x = 0$ and 0.1) were obtained using a high resolution scanning electron microscope (JEOL, JSM-7600F), operating at an accelerating voltage of 5 kV. The EDS facility attached to the SEM gave the elemental data on the samples. The structural properties of the samples were investigated by X-ray diffraction analysis using

a PANalytical X'Pert PRO PW3040/60 X-ray diffractometer with a Ni filtered Cu-K α ($\lambda = 0.154$ nm) monochromated radiation source. Data were collected in the 2θ range of 10–90° at a scan rate of 2° min^{−1}. The XPS data were analyzed using the XPS Peak 4.1 program.

Cell fabrication and electrochemical analysis

Electrochemical cells were fabricated as follows: coin cells of 2032 were assembled using lithium metal as anode, Celgard 2400 as separator and a 1 M solution of LiPF₆ in ethylene carbonate (EC), diethyl carbonate (DEC), dimethyl carbonate (DMC) (1 : 1 : 1, by volume) the electrolyte. The cathode was made from a slurry using a coating procedure from a mix containing active material powder, conducting black and poly(vinylidene fluoride) binder in *N*-methyl-2-pyrrolidone in the proportion 80 : 10 : 10, respectively. The slurry was coated over aluminium foil and dried at 110 °C overnight for 12 h. The 18 mm diameter slurry-coated aluminium foil electrodes were punched out and used as cathode. Coin cells were assembled in an argon filled glove box (MBraun, Germany) with moisture and oxygen levels maintained at less than 1 ppm. The charge-discharge cycles of the cells were carried out between 3.5–4.8 V at 0.2C rate with respect to their corresponding theoretical capacities of LiMn_2O_4 and $\text{LiMn}_{1.9}\text{Ni}_{0.1}\text{O}_4$ using a Maccor 4000 series 96-channel battery tester. The electrochemical impedance spectroscopy studies were carried out using a Bio-Logic VMP 3 Potentiostat/Galvanostat controlled by EC-Lab v10.40 software. EIS data were collected after ageing the fabricated lithium-ion cell for 24 h. Nyquist plots of the charged and discharged electrodes were recorded after allowing 1 h of stabilization.

Results and discussion

Morphological and EDS elemental analysis

Fig. 1a and b shows SEM images of LiMn_2O_4 and $\text{LiMn}_{1.9}\text{Ni}_{0.1}\text{O}_4$ samples, respectively. The SEM image in Fig. 1b shows that the $\text{LiMn}_{1.9}\text{Ni}_{0.1}\text{O}_4$ cathode materials have octahedral shape with clearly exposed (111) facets. The (111) facets are known to allow the formation of a thinner solid electrolyte interphase (SEI) than other facets thereby enhancing the Li-ion kinetics and cycling performance.²³

The estimated particle size distribution²⁴ of the compositions LiMn_2O_4 , and $\text{LiMn}_{1.9}\text{Ni}_{0.1}\text{O}_4$ is graphically presented in Fig. 1. Fig. 1c and d indicates that the particle sizes of the cathode materials are in the range of 0.30–0.50 μm for LiMn_2O_4 and 0.80–1.80 μm for $\text{LiMn}_{1.9}\text{Ni}_{0.1}\text{O}_4$. The calculated average particle sizes of the samples LiMn_2O_4 and $\text{LiMn}_{1.9}\text{Ni}_{0.1}\text{O}_4$ are 0.405 and 1.332 μm , respectively.

Energy-dispersive X-ray spectroscopy (EDS) elemental analysis was carried out in order to confirm the doping of Ni-ions. Table 1 displays the EDS elemental percentage of the samples. The EDS confirms that pristine LiMn_2O_4 and Ni-doped $\text{LiMn}_{1.9}\text{Ni}_{0.1}\text{O}_4$ spinel cathode materials were successfully synthesized using our aqueous reduction techniques. The EDS indicated that the nickel elemental quantity increases from 0.06



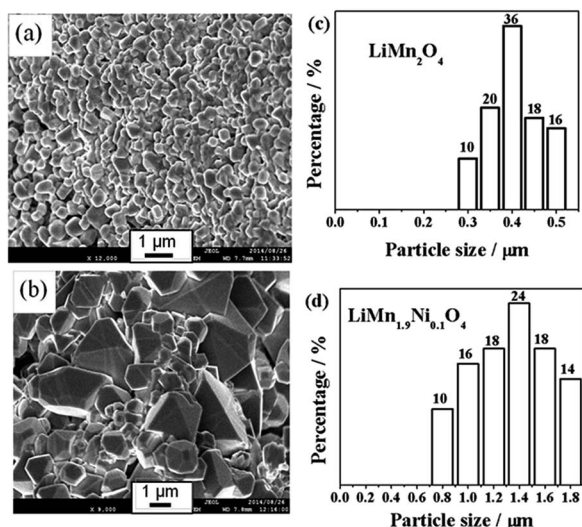


Fig. 1 Top-view SEM images of the products (a) LiMn_2O_4 and (b) $\text{LiMn}_{1.9}\text{Ni}_{0.1}\text{O}_4$; particle size distributions of the cathode materials (c) LiMn_2O_4 and (d) $\text{LiMn}_{1.9}\text{Ni}_{0.1}\text{O}_4$ from the SEM images.

for pristine LiMn_2O_4 to 1.62 for nickel substituted $\text{LiNi}_{0.1}\text{Mn}_{1.9}\text{O}_4$. The presence of carbon is due to the graphite-coating used in the SEM analysis.

Structural characterisation

The X-ray diffraction patterns to analyse the crystallographic structure and the impurity phases of the doped compounds synthesized by the aqueous reduction process are shown in Fig. 2. It is confirmed from the XRD patterns that the spinel LiMn_2O_4 phase (JCPDS File no. 88-1749) which indexes to a cubic spinel structure with a space group $Fd3m$ is formed for both pristine LiMn_2O_4 and nickel substituted $\text{LiMn}_{1.9}\text{Ni}_{0.1}\text{O}_4$ samples. The calculated lattice constants of LiMn_2O_4 and $\text{LiMn}_{1.9}\text{Ni}_{0.1}\text{O}_4$ are 8.239 and 8.234 Å respectively. The decrease in the lattice constant of the $\text{LiMn}_{1.9}\text{Ni}_{0.1}\text{O}_4$ is due to the replacement of the Mn^{3+} of high ionic radius ($r(\text{Mn}^{3+}) = 72.0$ pm) with Ni of smaller ionic radius (62.0 pm). Also, the XRD data for the precursor EMD, LiMn_2O_4 and $\text{LiMn}_{1.9}\text{Ni}_{0.1}\text{O}_4$ before 780 °C heat treatment are shown in Fig. 2b. The XRD peaks shifted slightly towards left with respect to EMD precursor reflection peaks, indicating structural change due to aqueous reduction reaction.

Fig. 3a and b shows the detailed XPS spectra of the Mn $2p_{3/2}$ peaks of the LiMn_2O_4 and $\text{LiMn}_{1.9}\text{Ni}_{0.1}\text{O}_4$ samples, respectively. There is a broad peak width for both the materials, which indicates that the Mn exist in more than one oxidation state. The deconvoluted peaks of Mn $2p_{3/2}$ for the samples LiMn_2O_4 and $\text{LiMn}_{1.9}\text{Ni}_{0.1}\text{O}_4$ with the obtained binding energy positions

Table 1 The elemental quantities of the samples obtained using EDS

Sample	C K	O K	Mn K	Ni K	Total%
LiMn_2O_4	15.89	31.98	52.08	0.06	100
$\text{LiMn}_{1.9}\text{O}_4$	8.68	40.80	48.86	1.62	100

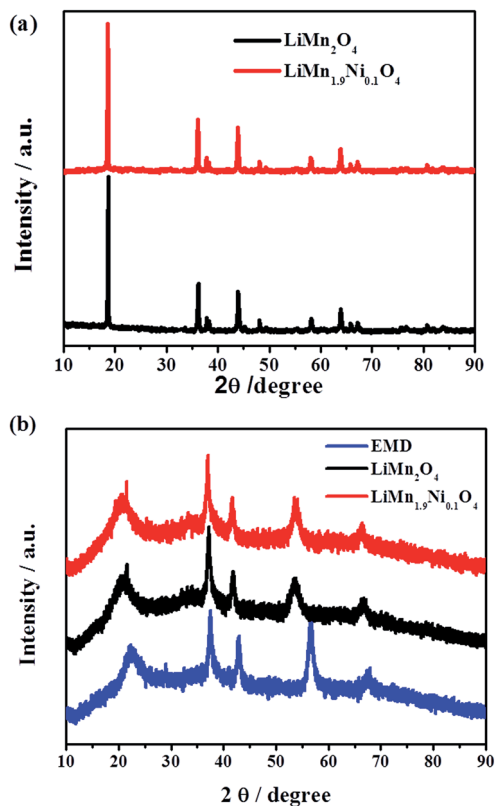


Fig. 2 X-ray diffraction patterns for the (a) LiMn_2O_4 and $\text{LiMn}_{1.9}\text{Ni}_{0.1}\text{O}_4$ (b) EMD, LiMn_2O_4 and $\text{LiMn}_{1.9}\text{Ni}_{0.1}\text{O}_4$ before 780 °C calcination.

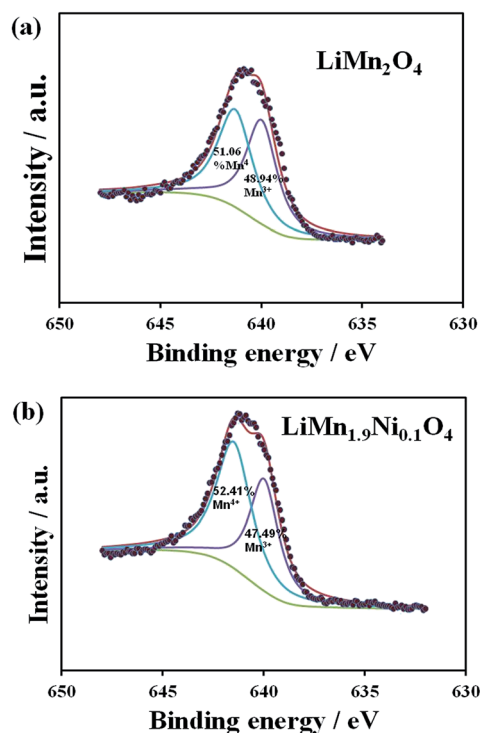


Fig. 3 The X-ray photoelectron spectra of the (a) LiMn_2O_4 and (b) $\text{LiMn}_{1.9}\text{Ni}_{0.1}\text{O}_4$ showing the Mn $2p_{3/2}$ peak.

Table 2 XPS (Mn-2p_{3/2} spectra) data of the LiMn₂O₄ and LiMn_{1.9}–Ni_{0.1}O₄ samples

Sample	Binding energy position (eV)		Cation distribution		Mn valence
	Mn ⁴⁺	Mn ³⁺	Mn ⁴⁺ (%)	Mn ³⁺ (%)	
LiMn ₂ O ₄	641.3	639.99	51.06	48.94	3.51
LiMn _{1.9} Ni _{0.1} O ₄	641.5	640.0	52.51	47.49	3.53

and cation distribution are summarised in Table 2. The binding energy peak positions corresponding to Mn⁴⁺ and Mn³⁺ are in agreement with previously reported values in the literature.²⁵ The XPS results indicate a decrease in the Mn³⁺ for the Ni-doped LiMn_{1.9}Ni_{0.1}O₄ cathode material that confirms a possible substitution of the Mn³⁺ by the Ni ions^{26,27} and results in increase in Mn valence from 3.51 of LiMn₂O₄ to 3.53 of LiMn_{1.9}Ni_{0.1}O₄. This slight increase in Mn valence is needed for stabilising the spinel structure and suppressed the John–Teller distortion associated to capacity fading.²⁷

Electrochemical performance

Galvanostatic charge/discharge experiments. The main objective of Ni substitution into a spinel LiMn₂O₄ cathode using small amounts of Ni is to achieve an improved electrochemical performance. The successful doping with nickel which was confirmed from the EDS, XRD and XPS data as described above,

is indeed reaffirmed by an improvement in the electrochemical performance.

The electrochemical activity role is played by Mn³⁺ in the pristine LiMn₂O₄. In the synthesized spinel, the Mn oxidation state is 3.5+ since an equal number of Mn³⁺ and Mn⁴⁺ are assumed to be present before charging. During charging, all Mn³⁺ convert ideally to Mn⁴⁺ by driving all Li⁺ ions into the anode electrode. The dissolution of manganese into the electrolyte is generated by the occurrence of the disproportionation reaction 2Mn³⁺ (solid) → Mn⁴⁺ (solid) + Mn²⁺ (solution) in^{10,11} the 4 V region. As a result the electrochemical active Mn³⁺ will diminish accordingly the discharge capacity will start to fade.

The galvanostatic charge/discharge capacity performance of the cathode materials was carried out at 0.2C rates with respect to their corresponding theoretical capacities. The representative 1st, 2nd, and 40th cycle charge/discharge capacities of LiMn_{2–x}Ni_xO₄ (x = 0 and 0.1) are displayed in Fig. 4. During the first cycle the as-synthesized cathode materials LiMn₂O₄, and LiMn_{1.9}Ni_{0.1}O₄ respectively delivered discharge capacities of 137 mA h g^{–1} and 128 mA h g^{–1}. The result shows that the initial discharge capacity decreases for the nickel-doped sample as expected. This trend of decrease in capacity is as a result of a reduction in the reversibly extractable Li⁺ ions from 1 for pristine LiMn₂O₄ to 1 – x for Ni-substituted lithium manganese oxides upon substitution of the electrochemically active Mn³⁺ ions.²⁸ The discharge capacities of the as-synthesized cathode materials are comparable to experimentally reported values.^{29,30}

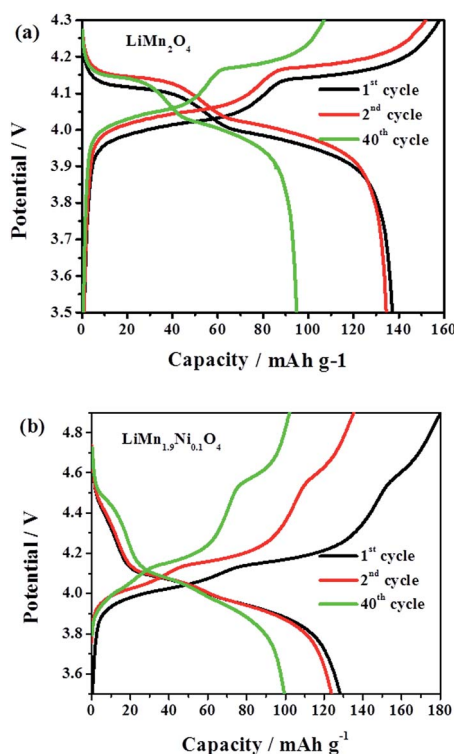


Fig. 4 The 1st, 2nd, and 40th cycle charge–discharge capacities of synthesized spinel (a) LiMn₂O₄ and (b) LiMn_{1.9}Ni_{0.1}O₄ cathode materials obtained at 0.2C.

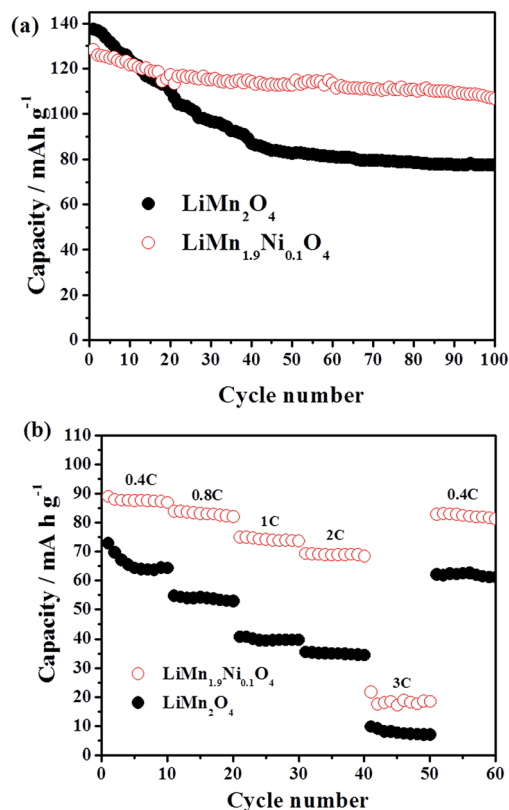


Fig. 5 The discharge capacity vs. cycle number for LiMn₂O₄ and LiMn_{1.9}Ni_{0.1}O₄ at (a) 0.2C and (b) 0.4, 0.8, 1, 2, 3C.



Despite that nickel insertion into EMD is difficult, it is interesting to see that our synthesis protocol was able to insert some amount that could successfully suppress the capacity fading. The capacity contribution at high voltage 4.5–4.7 V due to $\text{Ni}^{2+}/\text{Ni}^{4+}$ is very little, most of the electrochemical capacity is at the 4.1 V due to the $\text{Mn}^{3+}/\text{Mn}^{4+}$ redox couple. In addition, the first cycle charge–discharge reversibility for the samples LiMn_2O_4 and $\text{LiMn}_{1.9}\text{Ni}_{0.1}\text{O}_4$ is 86.9% and 69.7%, respectively. By considering the 2nd and 40th cycle capacity, it is noted that $\text{LiMn}_{1.9}\text{Ni}_{0.1}\text{O}_4$ shows gain in charge–discharge reversibility of 87% and 96% at the 2nd and 40th cycle, respectively. The improvement in reversibility arises from structural stability; at the 1–2 cycles, the spinel cathode material is not properly equilibrated with the electrolyte, but this should be expected to improve upon repetitive cycling, and hence the improved reversibility.

Cycling stability and rate capability. To compare the performance of the two spinel materials, we first examined their cycling performance at 100 cycles at constant rate (0.2C). As evident in Fig. 5a, the nickel-substituted sample, $\text{LiMn}_{1.9}\text{Ni}_{0.1}\text{O}_4$, exhibited high cycling performance compared to its pristine counterpart. The capacity retention of $\text{LiMn}_{1.9}\text{Ni}_{0.1}\text{O}_4$ is about

84% compared to the 52% capacity retention recorded for the pristine LiMn_2O_4 after the 100 repetitive cycling at room temperature.

Next, we look at the rate capability of the two spinel materials by performing experiments at different high rates, from 0.4 to 3C (Fig. 5b). Upon completion of the rate capability experiments and the initial rate of 0.4C was repeated, $\text{LiMn}_{1.9}\text{Ni}_{0.1}\text{O}_4$ lost about 7% of its initial capacity (*ca.* 90 vs. 84 mA h g^{−1}) while the LiMn_2O_4 experienced a loss of about 16% (*ca.* 74 vs. 62 mA h g^{−1}), clearly confirming the improved electrochemical stability due to the presence of the Ni in the $\text{LiMn}_{1.9}\text{Ni}_{0.1}\text{O}_4$. Also, in all cases, the capacity of the $\text{LiMn}_{1.9}\text{Ni}_{0.1}\text{O}_4$ is almost double to that of the LiMn_2O_4 ; for example at 1C, the capacities of the $\text{LiMn}_{1.9}\text{Ni}_{0.1}\text{O}_4$ and LiMn_2O_4 are approximately 78 and 40 mA h g^{−1}, respectively.

To further prove the stability of $\text{LiMn}_{1.9}\text{Ni}_{0.1}\text{O}_4$, we carried out SEM analysis after 100 cycles. From the SEM images of LiMn_2O_4 (Fig. 6a) and $\text{LiMn}_{1.9}\text{Ni}_{0.1}\text{O}_4$ (Fig. 6b) samples after 100 cycles, it is interesting to observe that the morphology of the $\text{LiMn}_{1.9}\text{Ni}_{0.1}\text{O}_4$ showed a microporous but inter-connected network structures compared to the morphology of the LiMn_2O_4 that showed huge agglomeration of the starting nanoparticles. The morphology of the $\text{LiMn}_{1.9}\text{Ni}_{0.1}\text{O}_4$ should allow for a more facile electrochemistry (in terms of stability and kinetics) than that of the agglomerated. From the above experimental findings, we can conclude that the high electrochemical performance of the $\text{LiMn}_{1.9}\text{Ni}_{0.1}\text{O}_4$ over its pristine counterpart LiMn_2O_4 can be related to a considerable decrease in the Jahn–Teller distortion spinel.^{15,31}

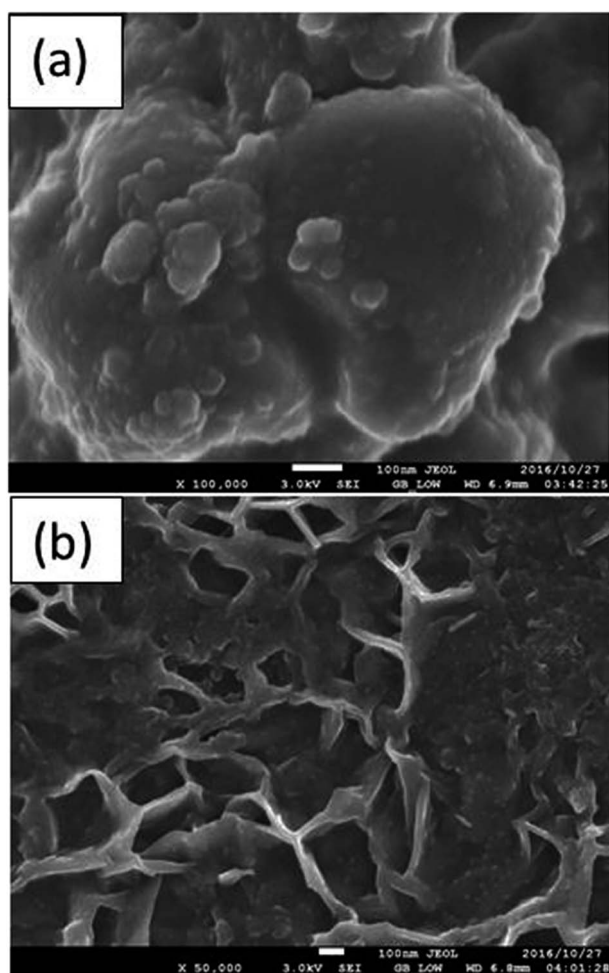


Fig. 6 The SEM images of the (a) LiMn_2O_4 and (b) $\text{LiMn}_{1.9}\text{Ni}_{0.1}\text{O}_4$ after 100 cycles at 0.2C.

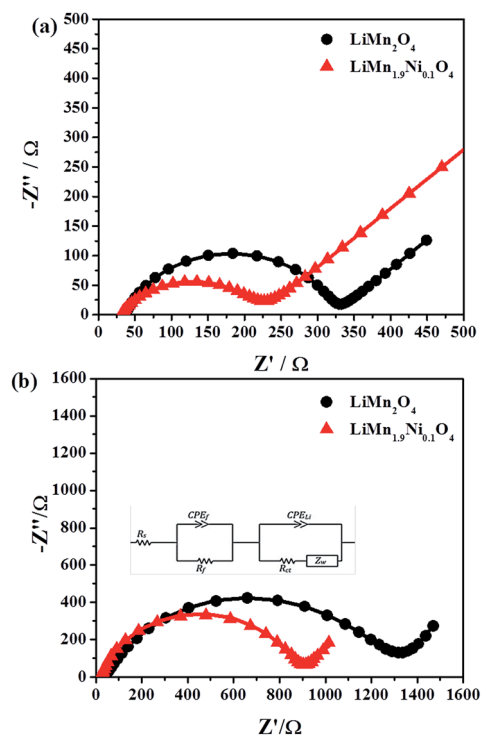


Fig. 7 Electrochemical impedance spectrum for LiMn_2O_4 and $\text{LiMn}_{1.9}\text{Ni}_{0.1}\text{O}_4$ samples (a) before, (b) after 100 cycles, and inset the equivalent circuit used to interpret the impedance spectra.



Table 3 Fitting results of Nyquist plots of as-synthesized $\text{LiNi}_x\text{Mn}_{2-x}\text{O}_4$ ($x = 0, 0.1$) cathode materials

	R_s (Ω)	R_f (Ω)	CPE_f (μF)	n	CPE_{dl} (mF)	R_{ct} (Ω)	Z_w ($\Omega \text{ s}^{-1/2}$)
Before 100 cycles							
LiMn_2O_4	37.04 ± 0.72	25.85 ± 2.32	15.17 ± 0.96	0.84 ± 0.13	28.37 ± 2.89	373.1 ± 2.68	42.62 ± 2.51
$\text{LiMn}_{1.9}\text{Ni}_{0.1}\text{O}_4$	33.82 ± 0.23	21.51 ± 0.95	73.54 ± 3.26	0.56 ± 0.21	58.42 ± 8.26	235.8 ± 1.78	86.79 ± 3.57
After 100 cycles							
LiMn_2O_4	28.05 ± 1.66	304 ± 2.57	32.95 ± 2.04	0.77 ± 0.18	16.61 ± 4.56	1105 ± 2.34	17.54 ± 0.78
$\text{LiMn}_{1.9}\text{Ni}_{0.1}\text{O}_4$	24.92 ± 3.19	277.9 ± 1.69	28.77 ± 3.6	0.68 ± 0.05	27.29 ± 9.76	431.8 ± 7.94	11.38 ± 0.57

Electrochemical impedance spectroscopy. Electrochemical impedance spectroscopy is a powerful technique to study the kinetics of lithium intercalation/de-intercalation processes. EIS was carried out to examine the electrode resistance changes for LiMn_2O_4 and nickel substituted $\text{LiMn}_{1.9}\text{Ni}_{0.1}\text{O}_4$ samples synthesized using nickel sulphate as nickel source. The Nyquist plots of pristine LiMn_2O_4 and $\text{LiMn}_{1.9}\text{Ni}_{0.1}\text{O}_4$ are presented in Fig. 7 and the equivalent circuit used is shown in Fig. 7b inset. The intercept at the real (Z') axis in high frequency corresponds to the series resistance due to anode-separator-electrolyte-cathode (R_s). The R_f and CPE_f are the surface film resistance and film capacitance. The semicircle in the middle frequency range indicates the charge transfer resistance (R_{ct}) and CPE_{dl} is the double layer capacitance at the electrolyte-electrode interface. The inclined straight line relates to the Warburg impedance (Z_w)³² and represents the diffusion impedance. The parameters of the equivalent circuit obtained from computer simulations for the as-synthesized LiMn_2O_4 and $\text{LiMn}_{1.9}\text{Ni}_{0.1}\text{O}_4$ is shown in Table 3. Using the fitting, the R_{ct} value of the LiMn_2O_4 and $\text{LiMn}_{1.9}\text{Ni}_{0.1}\text{O}_4$ samples were found to be 373 and 235 Ω (before 100 cycles), 1105 and 431 Ω (after 100 cycles), respectively. These results confirm that the nickel substitution suppressed the charge transfer resistance, which contributed to a higher discharge capacity and better capacity retention after 100 cycles compared to the pristine LiMn_2O_4 sample. Molecules with smaller particles are expected to give better electrochemical kinetics. It is surprising therefore to observe that $\text{LiMn}_{1.9}\text{Ni}_{0.1}\text{O}_4$ with larger average particle size (1.332 μm) gave an enhanced kinetics compared to the LiMn_2O_4 (0.405 μm). The

interpretation may be found from the SEM images of the two electrodes where the morphology of $\text{LiMn}_{1.9}\text{Ni}_{0.1}\text{O}_4$ showed porous and inter-connected networks that allow for electrochemistry to occur more effectively than an agglomerated and bulky morphology.

Plots of $-Z''$ vs. $\omega^{-1/2}$ for $\text{LiMn}_{2-x}\text{Ni}_x\text{O}_4$ ($x = 0, 0.1$) is shown in Fig. 8. The diffusion coefficients for LiMn_2O_4 and $\text{LiMn}_{1.9}\text{Ni}_{0.1}\text{O}_4$ cathode materials are 6.4×10^{-12} and $6.89 \times 10^{-11} \text{ cm}^2 \text{ s}^{-1}$ at room temperature, respectively. The result confirms that nickel substitution has significantly enhanced the Li^+ ion diffusion, which is a magnitude higher for nickel substituted $\text{LiMn}_{1.9}\text{Ni}_{0.1}\text{O}_4$ than the pristine LiMn_2O_4 diffusion coefficient.

Conclusions

In summary, we employed low-cost manganese precursor electrolytic manganese dioxide (EMD) and a low temperature aqueous reduction synthesis technique to successfully prepare nickel substituted spinel $\text{LiMn}_{2-x}\text{Ni}_x\text{O}_4$ ($x = 0$ and 0.1) cathode for lithium-ion battery by using $\text{NiSO}_4 \cdot 6\text{H}_2\text{O}$ as nickel source. We have confirmed that the Ni-ions substituted the Mn-ions using XRD, EDS, XPS and electrochemical performance studies. The nickel-substituted sample $\text{LiMn}_{1.9}\text{Ni}_{0.1}\text{O}_4$ exhibited superior capacity retention as compared to pristine LiMn_2O_4 ; $\text{LiMn}_{1.9}\text{Ni}_{0.1}\text{O}_4$ retained 84% of its initial capacity whereas pristine LiMn_2O_4 retained only 52% of its initial capacity.

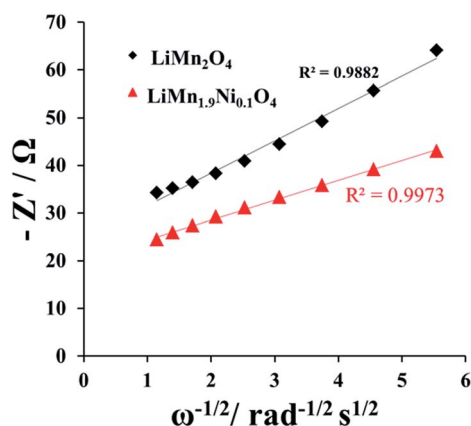
The study shows that the use of a small amount of Ni to eliminate the Jahn-Teller effects of the LiMn_2O_4 . In addition, this synthesis protocol has a great potential to be deployed for upscale-up production of pristine and Ni-doped spinel LiMn_2O_4 cathode materials for lithium-ion battery applications from locally-sourced and low-cost manganese precursor.

Acknowledgements

This work was supported by the CSIR. NK thanks the CSIR for PhD studentship.

References

- 1 K. Ding, J. Zhao, J. Zhou, Y. Zhao, Y. Chen, L. Liu, L. Wang, X. He and Z. Guo, *Mater. Chem. Phys.*, 2016, **177**, 31–39.
- 2 L. Wang, C. Yang, S. Dou, S. Wang, J. Zhang, X. Gao, J. Ma and Y. Yu, *Electrochim. Acta*, 2016, **219**, 592–603.
- 3 H. Lyu, J. Liu, S. Qiu, Y. Cao, C. Hu, S. Guo and Z. Guo, *J. Mater. Chem. A*, 2016, **4**, 9881–9889.

Fig. 8 Plots of $-Z''$ vs. $\omega^{-1/2}$ for LiMn_2O_4 and $\text{LiMn}_{1.9}\text{Ni}_{0.1}\text{O}_4$.

- 4 S. Qiu, G. Lu, J. Liu, H. Lyu, C. Hu, B. Li, X. Yan, J. Guo and Z. Guo, *RSC Adv.*, 2015, **5**, 87286–87294.
- 5 H. Cao, X. Wang, H. Gu, J. Liu, L. Luan, W. Liu, Y. Wang and Z. Guo, *RSC Adv.*, 2015, **5**, 34566–34571.
- 6 R. Santhanam and B. Rambabu, *J. Power Sources*, 2010, **195**, 5442–5451.
- 7 S. Patoux, L. Sannier, H. Lignier, Y. Reynier, C. Bourbon, S. Jouanneau, F. Le Cras and S. Martinet, *Electrochim. Acta*, 2008, **53**, 4137–4145.
- 8 T. Ohzuku, S. Takeda and M. Iwanaga, *J. Power Sources*, 1999, **81**, 90–94.
- 9 J. M. Amarilla, R. M. Rojas and J. M. Rojo, *J. Power Sources*, 2011, **196**, 5951–5959.
- 10 D. Aurbach, M. Levi, K. Gamulski, B. Markovsky, G. Salitra, E. Levi, U. Heider, L. Heider and R. Oesten, *J. Power Sources*, 1999, **81**, 472–479.
- 11 Y. Xia, Y. Zhou and M. Yoshio, *J. Electrochem. Soc.*, 1997, **144**, 2593–2600.
- 12 Y. Shin and A. Manthiram, *J. Electrochem. Soc.*, 2004, **151**, A204–A208.
- 13 B. Xu, D. Qian, Z. Wang and Y. S. Meng, *Mater. Sci. Eng., R*, 2012, **73**, 51–65.
- 14 M. Aklalouch, J. M. Amarilla, R. M. Rojas, I. Saadoune and J. M. Rojo, *Electrochem. Commun.*, 2010, **12**, 548–552.
- 15 M. A. Kebede, N. Kunjuzwa, C. J. Jafta, M. K. Mathe and K. I. Ozoemena, *Electrochim. Acta*, 2014, **128**, 172–177.
- 16 M. A. Kebede, M. J. Phasha, N. Kunjuzwa, L. J. le Roux, D. Mkhonto, K. I. Ozoemena and M. K. Mathe, *Sustainable Energy Technologies and Assessments*, 2014, **5**, 44–49.
- 17 H. Fang, Z. Wang, X. Li, H. Guo and W. Peng, *Mater. Lett.*, 2006, **60**, 1273–1275.
- 18 X. Qiu, X. Sun, W. Shen and N. Chen, *Solid State Ionics*, 1997, **93**, 335–339.
- 19 L. H. Chi, N. N. Dinh, S. Brutti and B. Scrosati, *Electrochim. Acta*, 2010, **55**, 5110–5116.
- 20 C. J. Jafta, M. K. Mathe, N. Manyala, W. D. Roos and K. I. Ozoemena, *ACS Appl. Mater. Interfaces*, 2013, **5**, 7592–7598.
- 21 D. Wang, I. Belharouak, G. M. Koenig, G. Zhou and K. Amine, *J. Mater. Chem.*, 2011, **21**, 9290–9295.
- 22 V. G. Kumar, J. Gnanaraj, S. Ben-David, D. M. Pickup, E. R. Van-Eck, A. Gedanken and D. Aurbach, *Chem. Mater.*, 2003, **15**, 4211–4216.
- 23 B. Hai, A. K. Shukla, H. Duncan and G. Chen, *J. Mater. Chem. A*, 2013, **1**, 759–769.
- 24 J. Gu, X. Yang, C. Li and K. Kou, *Ind. Eng. Chem. Res.*, 2016, **55**, 10941–10946.
- 25 K. Raju, F. P. Nkosi, E. Viswanathan, M. K. Mathe, K. Damodaran and K. I. Ozoemena, *Phys. Chem. Chem. Phys.*, 2016, **18**, 13074–13083.
- 26 Y. Wang, G. Yang, Z. Yang, L. Zhang, M. Fu, H. Long, Z. Li, Y. Huang and P. Lu, *Electrochim. Acta*, 2013, **102**, 416–422.
- 27 X. Li, Y. Xu and C. Wang, *Appl. Surf. Sci.*, 2009, **255**, 5651–5655.
- 28 H. Wu, J. Tu, X. Chen, Y. Li, X. Zhao and G. Cao, *J. Solid State Electrochem.*, 2007, **11**, 173–176.
- 29 Y. Ito, Y. Idemoto, Y. Tsunoda and N. Koura, *J. Power Sources*, 2003, **119**, 733–737.
- 30 X. Gu, X. Li, L. Xu, H. Xu, J. Yang and Y. Qian, *Int. J. Electrochem. Sci.*, 2012, **7**, 2504–2512.
- 31 B. Hwang, R. Santhanam and D. Liu, *J. Power Sources*, 2001, **97**, 443–446.
- 32 M. Levi and D. Aurbach, *J. Phys. Chem. B*, 1997, **101**, 4630–4640.

